Title

Tolerance to structural disorder and tunable mechanical behavior in self-assembled superlattices of polymer-grafted nanocrystals

Journal

Proceedings of the National Academy of Sciences of the United States of America, 114(11)

ISSN

0027-8424

Authors

Gu, X Wendy
Ye, Xingchen
Koshy, David M
et al.

Publication Date

2017-03-14

DOI

10.1073/pnas.1618508114

Peer reviewed

Tolerance to structural disorder and tunable mechanical behavior in self-assembled superlattices of polymer-grafted nanocrystals

X. Wendy Gu[a], Xingchen Ye[a], David M. Koshy[b], Shraddha Vachhani[c], Peter Hosemann[d], and A. Paul Alivisatos[a,e,f,g,1]

[a]Department of Chemistry, University of California, Berkeley, CA 94720; [b]Department of Chemical and Biomolecular Engineering, University of California, Berkeley, CA 94720; [c]Hysitron Inc., Minneapolis, MN 55344; [d]Department of Nuclear Engineering, University of California, Berkeley, CA 94720; [e]Department of Materials Science and Engineering, University of California, Berkeley, CA 94720; [f]Materials Science Division, Lawrence Berkeley National Laboratory, Berkeley, CA 94720; and [g]Kavli Energy NanoScience Institute, University of California, Berkeley and Lawrence Berkeley National Laboratory, Berkeley, CA 94720

Edited by William D. Nix, Stanford University, Stanford, CA, and approved January 30, 2017 (received for review November 8, 2016)

Large, freestanding membranes with remarkably high elastic modulus (>10 GPa) have been fabricated through the self-assembly of ligand-stabilized inorganic nanocrystals, even though these nanocrystals are connected only by soft organic ligands (e.g., dodecanethiol or DNA) that are not cross-linked or entangled. Recent developments in the synthesis of polymer-grafted nanocrystals have greatly expanded the library of accessible superlattice architectures, which allows superlattice mechanical behavior to be linked to specific structural features. Here, colloidal self-assembly is used to organize polystyrene-grafted Au nanocrystals at a fluid interface to form ordered solids with sub-10-nm periodic features. Thin-film buckling and nanoindentation are used to evaluate the mechanical behavior of polymer-grafted nanocrystal superlattices while exploring the role of polymer structural conformation, nanocrystal packing, and superlattice dimensions. Superlattices containing 3–20 vol % Au are found to have an elastic modulus of ∼6–19 GPa, and hardness of ∼120–170 MPa. We find that rapidly self-assembled superlattices have the highest elastic modulus, despite containing significant structural defects. Polymer extension, interdigitation, and grafting density are determined to be critical parameters that govern superlattice elastic and plastic deformation.

elasticity | buckling | nanocomposite | thin film | nanoindentation

Nanocrystal superlattices are ordered arrays of ligand-stabilized colloidal nanocrystals with unique thermal (1, 2), optical (3, 4), and electronic (5, 6) properties due to the nanoscale dimensions and periodic spacing of the inorganic crystals. Nanocrystal superlattices also exhibit superior mechanical performance: superlattice elastic modulus has been shown to rival that of lightweight structural composites (>10 GPa), and superlattice membranes are capable of withstanding repeated indents to large displacements (7–9). This is all the more remarkable because mechanical cohesion in the superlattices is attributed to van der Waals interactions between ligands on neighboring nanocrystals (10, 11), which are weak enough that the ligands are liquid at room temperature when not attached to nanocrystals. Superlattice strength and stiffness can be further elevated to values that are unprecedented for polymer nanocomposites by cross-linking the organic ligands that coat the nanocrystals (12). The unusual combination of physical properties in nanocrystal superlattices presents intriguing opportunities to use these materials as mechanically actuated optoelectronic sensors (13, 14), lightweight solar sails (15), and ultrathin barriers and coatings (16, 17), but warrants the development of a thorough understanding of the mechanical behavior of nanocrystal superlattices. In particular, the roles of nanocrystal packing geometry, ligand structural conformation, and ligand–ligand and ligand–nanocrystal interactions must be clarified to design multifunctional, self-assembled polymer nanocomposites with improved mechanical properties.

Recent advances in the synthesis of exceedingly monodisperse polymer-grafted nanocrystals have enabled the fabrication of one-component and binary nanocrystal superlattices with well-controlled long-range order (18). The nanocrystals used in these superlattices are grafted to short strands of polymer (∼10–200 monomers), and combine the structural versatility of polymers with the architectural control of superlattices. This class of superlattices provides an ideal framework for developing a mechanistic understanding of the novel mechanical properties of nanocrystal superlattices because superlattice structure, dimensions, and ligand length can be varied across a wide range of conditions and the effect of each of these parameters can be independently evaluated. In comparison, previous work showed that the elastic modulus, ductility, and hardness of nanocrystal arrays are influenced by ligand and nanocrystal type, and nanocrystal packing, but the alkyl ligands in these studies differed in length only by a few carbon–carbon bonds, and structural variations were not quantified (7, 9, 19–21). Polymer-grafted nanocrystal superlattices also differ from composites made from nanoparticles grafted to polymers with lengths of tens to thousands of monomers, because these composites usually contain aggregates or randomly dispersed nanoparticles instead of precisely ordered, periodic microstructures (22–27). In addition, chain entanglement plays a role in typical conventional polymer nanocomposites, but does not exist in nanocrystal superlattices containing short polymers. Here, we use thin-film buckling and nanoindentation to probe the elastic and plastic deformation of nanocrystal superlattices formed from Au nanocrystals grafted to short strands of polystyrene. The effect and interplay of superlattice structural disorder, sample dimensionality, nanocrystal spacing, and ligand length are revealed in this work.

Significance

Polymer nanocomposites containing nanoparticle fillers often have enhanced strength, stiffness, and toughness that are highly dependent on nanoparticle spatial distribution, which can be challenging to control in the limit of high nanoparticle loading. Solid superlattices formed from close-packed, ligand-coated inorganic nanocrystals can have high stiffness and large elastic recovery, although nanocrystals interact solely through van der Waals forces. We use polymer-grafted nanocrystals to make superlattices with versatile structural architecture and dimensions to investigate the effects of structural defects, film thickness, and polymer length on mechanical behavior. We find that the elastic response of the superlattice is large even when the arrangement of nanocrystals within the superlattice is perturbed, and that polymer conformation plays a large role in determining mechanical properties.

Author contributions: X.W.G. designed research; X.W.G., X.Y., D.M.K., and S.V. performed research; X.W.G., X.Y., D.M.K., P.H., and A.P.A. analyzed data; and X.W.G. and A.P.A. wrote the paper.

The authors declare no conflict of interest.

This article is a PNAS Direct Submission.

[1]To whom correspondence should be addressed. Email: paul.alivisatos@berkeley.edu.

This article contains supporting information online at www.pnas.org/lookup/suppl/doi:10.1073/pnas.1618508114/-/DCSupplemental.

Results and Discussion

Synthesis and Structural Characterization. Polystyrene-grafted Au (PS-Au) nanocrystals were synthesized following a previously published procedure (18). Thiol-terminated atactic polystyrene was introduced postsynthetically to replace the native oleylamine ligands on as-synthesized Au nanocrystals. PS-Au nanocrystals were self-assembled on a liquid interface to form superlattice thin films. A suspension of spherical PS-Au nanocrystals in toluene was drop-cast onto ethylene glycol contained in a Teflon trough. As the toluene evaporated, the nanocrystals coalesced to form thin films with millimeter to centimeter lateral dimensions, and thicknesses of a single monolayer to hundreds of nanometers. Films were self-assembled under four different drying rates: (*i*) over a period of ∼5 h by tightly sealing the Teflon well with glass slides (referred to hereafter as RT-covered); (*ii*) over ∼4 min by leaving the Teflon well open to air (RT-uncovered); (*iii*) over ∼2 min by depositing the Au-PS nanocrystals on ethylene glycol (EG) heated to 43 °C in a water bath (43 °C-uncovered); and (*iv*) in less than 1 min by depositing the Au-PS nanocrystals on EG heated to 58 °C (58 °C-uncovered). Superlattice periodicity was tuned by varying polystyrene molecular weight from 1.1 to 20 kg/mol while maintaining Au nanocrystal diameter (d) to be 5.2 ± 0.4 nm. Nanocrystal center-to-center distances (D) ranged from 8.6 ± 1.0 nm to 16.7 ± 2.1 nm, which corresponds to Au volume fractions of 20–3%, respectively (Table S1).

The structural conformation of the polystyrene grafted to the Au nanocrystals can be discussed in the context of polymer brushes, which are polymers that are connected to an interface at one end (28–31). Polymer brushes on curved surfaces can be classified as concentrated (almost full extension of polymer chains), semidilute (somewhat extended), or dilute (mushroom-like coils) polymer brushes depending on the radius of curvature of the surface, distance from the surface, polymer grafting density, and polymer chain length. The polymer brush regime can be determined by examining the scaling behavior of brush height, h, versus the degree of polymerization, N (32, 33). Brush height in solid films of polymer-grafted nanoparticles has been shown to scale as $h \sim N^{0.8}$ in the concentrated polymer brush regime, and $h \sim N^{0.5}$ in the semidilute polymer brush regime (24). Polymer brush height in the PS-Au superlattices was found to scale as $h \sim N^{0.5}$ (Fig. S1). This indicates that the polystyrene in the superlattices has the conformation of a semidilute polymer brush, suggesting that there is enough free volume in the polystyrene layer for other polymers to interdigitate with the grafted polystyrene. The interaction of the PS-Au nanocrystals is intermediate to that of hard spheres (as for fully dense polymer brushes with no interdigitation) and entangled polymers surrounding an inorganic core (as would be the case for longer polystyrene or lower grafting density). The polystyrene used in the PS-Au superlattices is too short for chain entanglement (34), so mechanical cohesion between these polymer-grafted nanocrystals is likely to arise through van der Waals forces (10, 11) and physically interlocked segments between interdigitated polymer strands. Thermogravimetric analysis (TGA) was performed on PS-Au nanocrystals to obtain the mass fraction of organic material in the superlattices. TGA revealed the presence of a significant amount of unbound polystyrene and oleylamine left over from nanocrystal synthesis (Fig. S2). This indicates that free polystyrene and oleylamine are codeposited with PS-Au nanocrystals during self-assembly, and are likely to act as homopolymers in interactions with polymer-grafted nanocrystals (25).

Freestanding membranes with lateral dimensions of up to ∼1.5 × 4.3 μm^2 and single nanocrystal thickness were formed by transferring the superlattice thin film from the liquid interface to a holey carbon transmission electron microscopy (TEM) grid (Fig. 1*A*). Cracks that likely formed during the transfer of the superlattice to the TEM grid consist of fracture along close-packed planes of nanocrystals and matching fracture surfaces (Fig. 1*B*). The appearance of these cracks is indicative of brittle fracture, and suggests the lack of significant plastic deformation before failure. Atomic force microscopy (AFM) was used to characterize superlattice film thickness (t) (Fig. 1 *C* and *D*). The thickness of a single monolayer was measured by suspending a superlattice film on a SiN membrane TEM grid, identifying and mapping monolayer regions in TEM, and then performing AFM on the edge of these monolayer regions. The film thickness was taken to be the difference between the height of the underlying substrate and the monolayer film (see Table S1 for monolayer thicknesses). The average thickness of monolayer films was found to be 80–92% of the average nanocrystal center-to-center distance, which indicates that polystyrene strands are slightly collapsed in the out-of-plane direction relative to their arrangement in the in-plane direction of the film. We believe that this asymmetry results from the unfavorable interaction of hydrophobic polystyrene with air and/or EG interfaces during superlattice self-assembly, similar to the case of the ligand shell asymmetry recently demonstrated in self-assembled superlattices formed from dodecanethiol-capped Au nanocrystals (35).

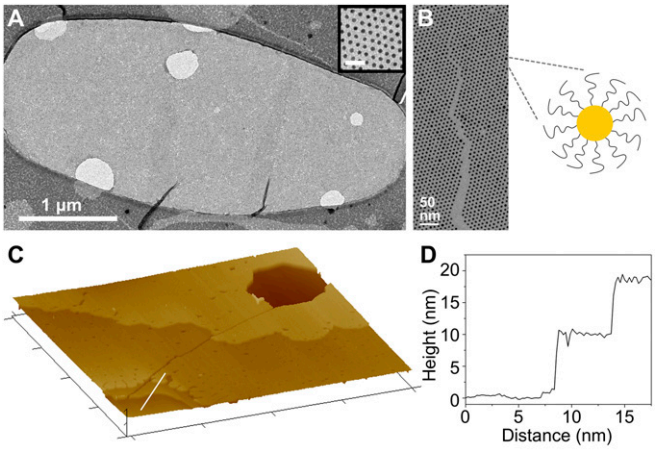

Fig. 1. Self-assembled nanocrystal superlattice thin films. (*A*) Low-magnification and high-magnification (*Inset*) TEM images of 3-kg/mol PS-Au freestanding monolayer film suspended on holey carbon mesh. (Scale bar on the inset image, 25 nm.) (*B*) Cracked superlattice showing the brittle nature of film and schematic of polymer-grafted nanocrystal. (*C*) AFM of 5-kg/mol PS-Au film on Si wafer (71 × 71 μm^2) and (*D*) height profile of slice traced along the white line in *C*.

Mechanical Behavior. The elastic behavior of PS-Au superlattice thin films was evaluated through a buckling-based method that has previously been validated for ultrathin polystyrene films (36, 37). Au-PS thin films were placed on polydimethylsiloxane (PDMS) blocks, which were compressed in a tensile tester mounted on an optical microscope. Elastic buckling occurred in the thin film at small strains (<10%) due to the elastic mismatch between the compliant PDMS and stiffer thin film (Fig. 2). The buckling wavelength, λ, was captured using optical microscopy and is related to the material properties and geometry of the thin film and substrate by

$$\frac{E_f}{\left(1-\upsilon_f{}^2\right)} = \frac{3E_s}{\left(1-\upsilon_s{}^2\right)}\left(\frac{\lambda}{2\pi t}\right)^3, \qquad [1]$$

where E_f and υ_f are elastic modulus and Poisson ratio of the thin film, E_s and υ_s are elastic modulus and Poisson ratio of the PDMS substrate, and t is film thickness. Eq. **1** derives the structural configuration that minimized the energy of a semiinfinite substrate, $E_s\lambda^3/(1-\upsilon_s{}^2)$, and the thin film, $E_f t^3/(1-\upsilon_f{}^2)$, in the limits of small strain, and large E_f/E_s. Eq. **1** can be rearranged to obtain E_f, and the thin-film bending modulus, $B = E_f t^3/(12(1-\upsilon_f{}^2))$, which represents the work required to bend a thin film. Eq. **1** applies to elastically homogeneous materials, which is an

ENGINEERING

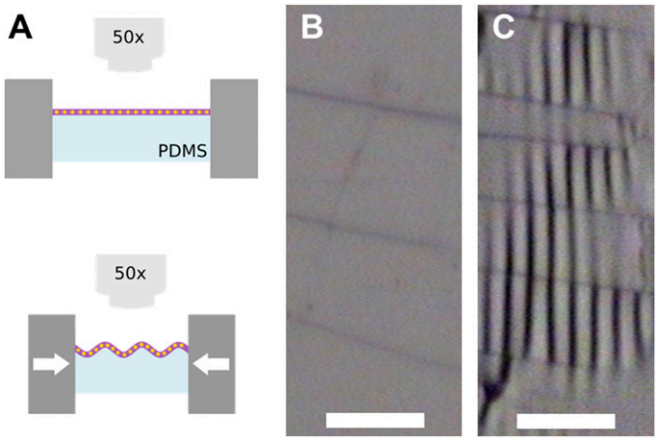

Fig. 2. Buckled superlattice thin films suspended on PDMS. (*A*) Schematic of the buckling measurement. The PS-Au film is placed on a PDMS substrate, which is compressed in a load cell. Buckles that develop in the PS-Au film due to the elastic mismatch between film and substrate are captured using an optical microscope. Optical micrographs of 5-kg/mol PS-Au superlattice thin film with thickness of ~40 nm (*B*) before and (*C*) after buckling. (Scale bars, 10 μm.)

assumption that does not apply to superlattices when their film thickness is comparable to nanocrystal size. After performing the buckling measurement, the film was unloaded and the film thickness was measured at each buckled region using AFM. These buckled regions returned to a flat geometry after the sample was unloaded, which confirms the elastic, reversible nature of the buckles. The elastically buckled regions are several micrometers to tens of micrometers wide. Crystalline grains within the superlattice film typically extend across no more than hundreds of nanometers (although an occasional, micrometer-scale grain may be found), therefore each buckling measurement samples several grains of differing orientation, and the measured properties correspond to polycrystalline values. Variations in the number of superlattice grains and the distribution of superlattice grain orientations that are sampled in a given buckling measurement are likely to contribute to scatter in the measured mechanical properties. The Poisson ratio, v, of the superlattice was calculated as the average of the values predicted by the Voigt (parallel) and Reuss (series) composite models, and ranged from 0.36 to 0.34 for 1.1–20 kg/mol PS-Au superlattices (38).

The bending and elastic moduli of the nanocrystal superlattices were investigated as a function of superlattice structural order. Three-kg/mol PS-Au superlattices were prepared under four different drying rates. A slower drying rate led to superlattices with large regions of hexagonal, close-packed nanocrystals and few defects, whereas faster drying rates led to superlattices with more grain boundaries, disclinations, vacancies, interstitials, and regions of nonuniform lattice spacing (Fig. 3 *A–D*). Superlattice structural order was characterized by determining the distribution of interparticle spacings from TEM images of the superlattices (Fig. 3 *E–H*). The interparticle spacing for the slowest drying, most highly ordered 3-kg/mol PS-Au superlattice (prepared at RT-covered) was 11.1 ± 0.7 nm, and increased to 11.8 ± 1.0 nm, 11.6 ± 1.2 nm, and 11.1 ± 1.6 nm for RT-uncovered, 43 °C-uncovered, and 58 °C-uncovered, respectively. The distribution of interparticle distance broadened monotonically with increased drying rate, from an SD of 6% of the average interparticle spacing in the slowest-drying films to 14% in the fastest-drying films, mostly due to the increase in the number of larger than average interparticle spacings. The density of point defects also increased monotonically from 2 point defects per 1,000 PS-Au nanocrystals for RT-covered superlattices, to 6, 11, and 28 point defects per 1,000 PS-Au

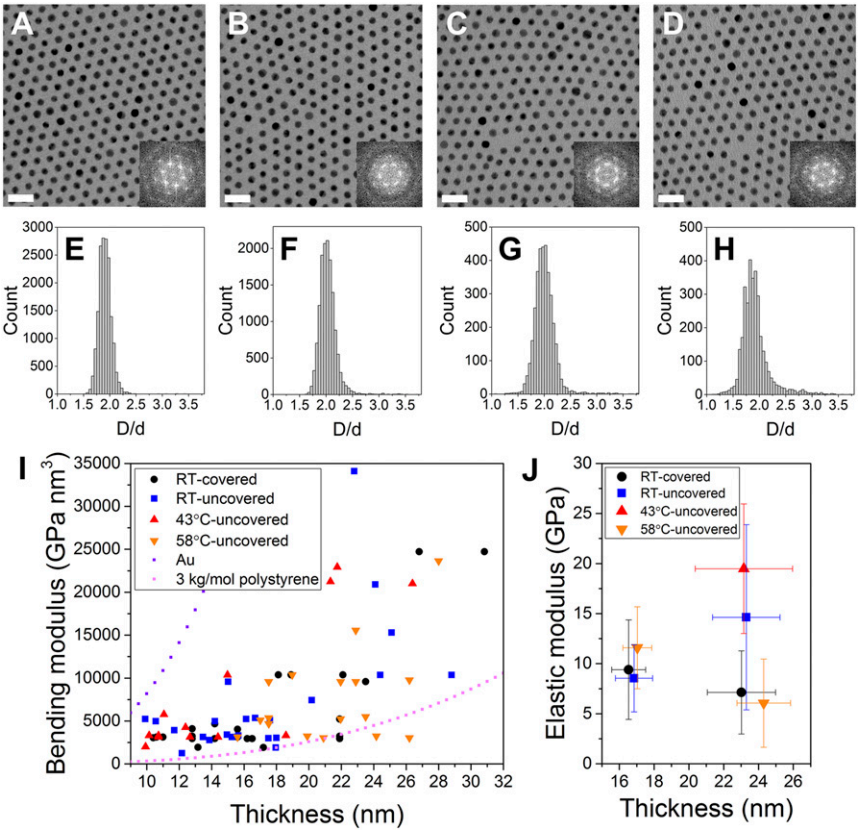

Fig. 3. Superlattice structure and mechanical behavior for 3-kg/mol PS-Au superlattices self-assembled at different drying rates. Representative (*A–D*) TEM images and (*E–H*) corresponding statistical analysis of the distribution of interparticle spacing for superlattice dried at (*A* and *E*) room temperature while covered with a glass slide (RT-covered); (*B* and *F*) RT-uncovered; (*C* and *G*) 43 °C-uncovered; and (*D* and *H*) 58 °C-uncovered. *E–H* are plotted as a function of particle center-to-center distance, *D*, over particle diameter, *d*. (Scale bars, 20 nm.) (*I*) Bending modulus of 3-kg/mol PS-Au superlattices and calculated bending modulus for bulk Au and 3-kg/mol PS based on literature values (37). (*J*) Elastic modulus of 3-kg/mol PS-Au superlattices with thicknesses equivalent to two and three superlattice layers.

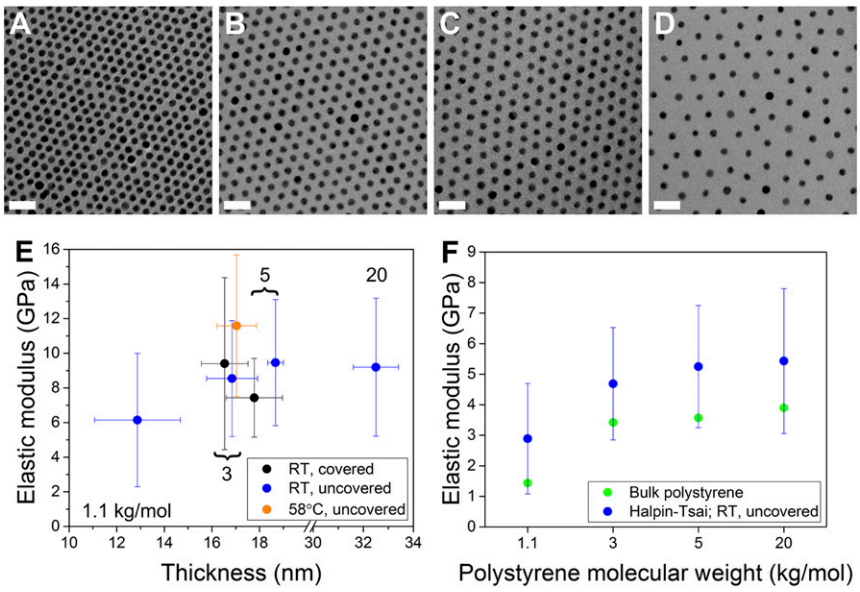

Fig. 4. Structure and elastic modulus of superlattices with varying polystyrene molecular weights. TEM images of (*A*) 1.1-kg/mol, (*B*) 3-kg/mol, (*C*) 5-kg/mol, and (*D*) 20-kg/mol PS-Au superlattice. (Scale bars, 20 nm.) (*E*) Elastic modulus of superlattices of two-layer thickness with different polystyrene molecular weights. (*F*) Comparison of the elastic modulus of bulk polystyrene with 1.1–20-kg/mol molecular weight (green data points) (from ref. 37), and the elastic modulus of the polymeric component of the superlattice calculated using the Halpin–Tsai model (blue data points).

nanocrystals for superlattices prepared at RT-uncovered, 43 °C-uncovered, and 58 °C-uncovered, respectively.

The bending modulus for 3-kg/mol PS-Au superlattices is plotted versus film thickness in Fig. 3*I*, and is also compared with the calculated bending modulus of bulk Au and bulk 3-kg/mol polystyrene with a thin-film geometry identical to that of the superlattices. Measured thicknesses did not always follow discrete values that correspond to superlattice layer thicknesses as shown in Fig. 1*D*. We believe that these intermediate thicknesses are due to the presence of small islands or holes in the superlattice that are below the resolution of the optical microscope used during the buckling measurements. These islands and holes have been observed in TEM and AFM over small scan areas (Fig. S3). Thus, the measured thickness for these uneven films is the average thickness of small patches of different superlattice layers. The nonuniform deposition of unbound polystyrene and oleylamine present in solution may add to the variations in measured thicknesses. This possibility is supported by our observation that superlattice films that have been identified as a single monolayer of nanocrystals using TEM were found to vary in thickness by ±2 nm in different regions. The bending modulus obtained from the buckling measurements shows a great deal of scatter, especially at larger thicknesses. We believe that this is due to increased variation in superlattice microstructure at larger thicknesses, such as variations in orientation between superlattice layers.

The superlattice bending modulus mostly fell between the bending modulus of bulk Au and bulk polystyrene, although a few data points fall below the bending modulus of bulk polystyrene. The bending modulus generally increases with increasing film thickness, although the bending modulus appears to plateau at thicknesses lower than 14 nm. Although intriguing, further investigation must be undertaken before strong conclusions can be made about the elastic properties of the superlattices at ultralow thicknesses, especially considering the uncertainty in the thickness measurement and the strong dependence of elastic modulus on thickness ($E \sim 1/t^3$). We speculate that the increase in bending modulus at low thicknesses may be due to the ligand shell asymmetry identified in superlattice monolayers using TEM and AFM. The contraction in ligand shell thickness in the out-of-plane direction relative to the in-plane dimensions in superlattice monolayers indicates that the polystyrene must be at a higher density at the surfaces of the superlattice, which may result in a higher stiffness. Indirect evidence for the high bending modulus in superlattice monolayers is provided by TEM images of superlattices that happened to be deposited in a cantilever-like geometry (supported along one edge only) on holey TEM grids (Fig. S4). These cantilever-like films appear to be stable under the electron beam and their own weight, unlike dodecanethiol-Au superlattice freestanding membranes (35). AFM membrane deflection experiments were also performed on superlattice monolayers suspended on holey SiN TEM grids. We found that repeated indents (up to 24) to large displacements did not damage the superlattice (Fig. S5).

Alternatively, the increase in bending modulus at low thicknesses may be due to increased bending stiffness as the sample thickness approaches intrinsic microstructural length scales. This size effect has been observed in dodecanethiol-Au superlattice films (39) and microfabricated cantilevers (40), and can be captured using advanced continuum elasticity theories that consider nonlocal stress–strain behavior (41, 42). The magnitude of this size effect can be evaluated by comparing the measured bending modulus and the bending modulus that is predicted using the elastic modulus of the bulk material (Fig. S6). Through this analysis, we find that the critical material length scale for the emergence of the bending size effect is about the thickness of a superlattice monolayer. These calculations indicate that increased bending modulus in superlattices with 1–3-layer thickness could be due to the breakdown of standard elasticity at the nanoscale.

Although standard elasticity does not strictly apply to few-layered superlattice films because of their heterogeneous microstructure, bending modulus was converted to elastic modulus using Eq. **1** for purposes of comparison between superlattices with different dimensions and structure. In this situation, elastic modulus represents the bending modulus normalized by the critical sample length scale rather than an intrinsic material parameter. The elastic modulus of 3-kg/mol PS-Au superlattices that correspond to two- (15–18.5 nm) and three-layer thicknesses (22.7–26.7 nm) are shown in Fig. 3*J*. The elastic modulus of two-layered superlattices increased from ∼9 GPa in RT-covered and RT-uncovered samples, to 11.6 ± 4.1 GPa for the 58 °C-uncovered sample. The elastic modulus of superlattices with three-layer thickness decreased to 7.1 ± 4.1 GPa for the RT-covered sample, and 6.1 ± 4.4 GPa in the 58 °C-uncovered sample, but increased to 14.6 ± 9.2 GPa in the RT-uncovered sample. Surprisingly, the 43 °C-uncovered sample with three-layer thickness had the highest elastic modulus of 19.5 ± 6.5 GPa. These results indicate that increased superlattice disorder does not have

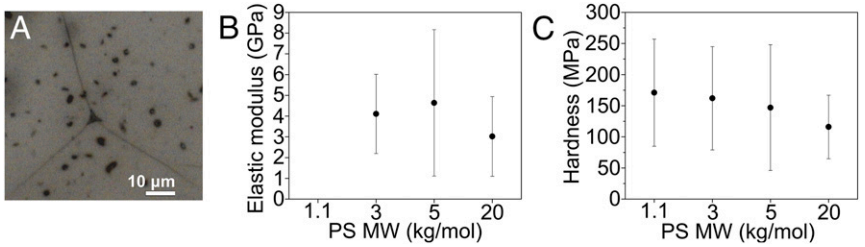

Fig. 5. Elastic modulus and hardness measured through nanoindentation. (*A*) Optical image of residual imprint left by nanoindentation into a 3-kg/mol PS-Au film. Cracks extend from the tips of the indentation. (*B*) Elastic modulus and (*C*) hardness of superlattice films with different polystyrene molecular weights.

a detrimental effect on elastic modulus, and could actually lead to an increase in elastic modulus up to a certain degree of disorder. A small increase in elastic modulus with increased lattice disorder was also observed in RT-covered and RT-uncovered 5-kg/mol PS-Au superlattices (Fig. 4*E*).

This relationship between elastic modulus and structural order is intriguing because metallic and inorganic crystalline solids tend to have similar or slightly higher elastic moduli than their glassy counterparts (43–45). We believe that the high elastic modulus in the 43 °C-uncovered, 3-kg/mol PS-Au superlattice could be because the grafted polystyrene and unbound polystyrene/oleylamine incorporated into the superlattice are frozen in nonequilibrium conformations during rapid drying. In this sense, the high elastic modulus can be attributed to compressive residual stress that resists further compression during the buckling measurement. To test this theory, the 43 °C-uncovered, 3-kg/mol PS-Au superlattice was thermally annealed above its glass transition temperature without disrupting the arrangement of Au nanocrystals within the superlattice (Fig. S7). The bending and elastic modulus of the annealed superlattice decreased dramatically (elastic modulus decreased to ∼1 GPa), which supports the idea that residual stress can lead to elevated moduli in fast-drying superlattices (Fig. S8). The glass transition temperature (T_g) of the 3-kg/mol PS-Au superlattice is estimated to be ∼86 °C, based on the T_g of bulk 3-kg/mol polystyrene and the T_g enhancement that has been observed in densely grafted polymer brushes (37, 46). Thus, residual stresses in the 3-kg/mol PS-Au superlattice are kinetically trapped on experimental time scales at room temperature. The enhancement in modulus due to residual stress appears to compensate for any reduction in modulus due to decreased local density of nanocrystals and decreased nearest-neighbor interactions between nanocrystals in disordered superlattices. We postulate that the high elastic modulus previously reported in freestanding self-assembled nanocrystal superlattices formed with short organic linkers like dodecanethiol and DNA may be influenced by their fast drying conditions (7–9). In contrast, studies on polystyrene or poly (methylmethacrylate)-grafted nanoparticle arrays do not show higher elastic moduli in disordered arrays because the nanoparticle composites are annealed and reach equilibrium configurations (24). Bending size effects due to the heterogeneous superlattice microstructure may also contribute to the elevated elastic modulus in fast-drying superlattices with 2–3-layer thickness.

The molecular weight of polystyrene was varied from 1.1 to 20 kg/mol, which resulted in superlattice elastic moduli of 6.1 ± 3.9 GPa to 11.6 ± 4.1 GPa for two-layered superlattices (Fig. 4). The elastic moduli measured here are comparable to the values for nanocrystal arrays containing short, alkyl ligands measured through AFM membrane deflection (7–9) and nanoindentation (19–21), and are higher than the modulus of polystyrene-grafted silica nanoparticle films with similar polymer molecular weight and concentrated polymer brushes (24). The Halpin–Tsai model was used to separate the contribution of the polymeric and inorganic components to the superlattice elastic modulus in superlattices prepared at RT-covered (38, 47). The Halpin-Tsai model predicts the elastic properties of composites by interpolating between upper and lower bounds for the elasticity of a matrix containing a particle or fiber obtained using self-consistent-field theory. The degree of reinforcement from the filler material is determined based on filler geometry and volume fraction. Using this model, the superlattice was taken to be a homogeneous, single-component polymeric matrix embedded with spherical Au nanocrystals. Superlattice elastic modulus, Au elastic modulus, and Au volume fraction were used to calculate the modulus of the matrix material, which was found to be 2.9 ± 1.8 GPa to 5.4 ± 2.4 GPa (Fig. 4*F*). This value is a factor of 1.4–2× higher than the elastic modulus of bulk polystyrene of the equivalent molecular weight.

Nanoindentation was performed on superlattice films with different polystyrene molecular weights. Films were prepared at RT-covered to make superlattice films with long-range order with thicknesses of 1–3 μm. Partial unloading tests were used to obtain elastic modulus and hardness at different depths into the film (Fig. S9). A Berkovich tip was used to indent the films at a strain rate of 0.02–0.04 s^{-1} to a maximum load of 5 mN. Cracks formed at the tips of the indentations made in the films, which provides further proof of the brittle nature of the superlattice films (Fig. 5*A*). Cracking is likely to have occurred at shallow depths during partial unloading tests, because cracks were also observed to form at indentations from quasi-static tests to depths of ∼200 nm. Substrate effects led to an increase in elastic modulus after indentation to more than ∼20% of film thickness, and an increase in hardness after indentation to 40% or more of film thickness (48). A significant indentation size effect was observed at shallow depths in the hardness measurement. Modulus and hardness were taken from depths at which indentation size effects, and substrate effects are minimal. Nanoindentation elastic modulus was lowest for the 20-kg/mol PS-Au film, and increased for 3-kg/mol and 5-kg/mol PS-Au films (Fig. 5*B*), which is similar to the trend in modulus obtained from the buckling measurements. Elastic modulus could not be accurately probed for the 1.1-kg/mol PS-Au film because of its limited thickness (∼1 μm). Hardness ranged from 116 ± 51 MPa to 171 ± 86 MPa, and increased with decreasing polystyrene molecular weight, which corresponds to increasing Au volume fraction (Fig. 5*C*). The elastic modulus measured using nanoindentation may be lower than the modulus measured using the buckling method because structural differences at surfaces of the superlattice may lead to higher modulus in films consisting of a few layers of nanocrystals. In addition, the formation of microscopic cracks near the tips of the indentation should lead to reductions in the measured modulus and hardness. Viscoelastic relaxation of the superlattice during unloading may also lead to a slight reduction in the measured elastic modulus. Slightly higher modulus and hardness were measured in the PS-Au superlattice films using nanoindentation, compared with polystyrene-grafted silica nanoparticle films with similar polystyrene molecular weight (24).

In summary, the elastic and plastic deformation of polystyrene grafted-Au nanocrystal superlattice thin films was investigated using elastic thin film buckling and nanoindentation. Superlattice bending modulus was determined for superlattices with thicknesses corresponding to 1–3 nanocrystal layers, and elastic modulus was extracted from bending modulus for multilayer films. Elastic modulus ranged from 6.1 ± 3.9 GPa to 19.5 ± 6.5 GPa for polystyrene molecular weight of 1.1–20 kg/mol, and varied with

the degree of superlattice structural disorder. The highest elastic modulus corresponds to a fairly disordered superlattice made with 3-kg/mol PS and self-assembled at 43 °C-uncovered, which indicates that increased structural disorder may actually correlate with increased superlattice elastic modulus. The hardness of superlattice films with different polystyrene molecular weights varied from 116 ± 51 MPa to 171 ± 86 MPa.

The mechanical behavior described here demonstrates a path forward for the fabrication of ultrathin films with high strength and stiffness using the self-assembly of colloidal nanocrystals. Our work indicates that the elastic modulus in nanocrystal superlattices can be made to rival the modulus of polymeric nanocomposites manufactured through complex and energy-intensive processes by reducing superlattice thickness, inducing an optimal degree of structural disorder, and judiciously choosing the polymer molecular weight. The ability to design mechanically robust superlattices would be improved by the development of advanced theories of polymer brushes, which are able to relate structural deformation to polymer brush conformation, and can predict structural evolution within polymer and ligand brush during highly nonequilibrium processes such as nanocrystal self-assembly. Our understanding of nanocrystal superlattice mechanical behavior would also be enriched by obtaining a full, tensile stress–strain curve for this material, to understand properties such as strength and fracture toughness, and by studying the time dependence of superlattice mechanical properties. To accomplish these goals, it is desirable to fabricate self-assembled nanocrystal arrays with bulk length scales, which remains a challenge in the field (8, 12, 49). Nevertheless, self-assembled nanocrystal superlattices are a rich model system for understanding mechanical behavior in materials under nanoscale confinement, and the properties of polymer nanocomposites.

Methods

A detailed description of experimental methods is included in *SI Methods*. PS-Au nanocrystals were self-assembled into superlattices through controlled drying on an EG interface. Buckling measurements were performed using a load frame (Psylotech) mounted on a confocal microscope (Witec). Nanoindentation was conducted with a Hysitron TI-950 Triboindenter in load-controlled mode.

ACKNOWLEDGMENTS. We thank Dr. Stefan Fischer for help with TGA and Prof. Ting Xu and Katherine Evans for AFM access. We deeply appreciate Prof. Ting Xu, Prof. Robert Ritchie, and Prof. Kenneth Shull for useful comments and discussion. We gratefully acknowledge financial support from the "Self-Assembly of Organic/Inorganic Nanocomposite Materials" Program, KC3104, Engineering and Technology Program, Office of Basic Energy Sciences of the US Department of Energy, under Contract DE-AC02-05CH11231.

1. Wang RY, et al. (2008) Enhanced thermopower in PbSe nanocrystal quantum dot superlattices. *Nano Lett* 8(8):2283–2288.
2. Ong WL, Rupich SM, Talapin DV, McGaughey AJH, Malen JA (2013) Surface chemistry mediates thermal transport in three-dimensional nanocrystal arrays. *Nat Mater* 12(5): 410–415.
3. Shevchenko EV, et al. (2008) Self-assembled binary superlattices of CdSe and Au nanocrystals and their fluorescence properties. *J Am Chem Soc* 130(11):3274–3275.
4. Ye X, Chen J, Diroll BT, Murray CB (2013) Tunable plasmonic coupling in self-assembled binary nanocrystal superlattices studied by correlated optical microspectrophotometry and electron microscopy. *Nano Lett* 13(3):1291–1297.
5. Urban JJ, Talapin DV, Shevchenko EV, Kagan CR, Murray CB (2007) Synergism in binary nanocrystal superlattices leads to enhanced p-type conductivity in self-assembled PbTe/Ag2 Te thin films. *Nat Mater* 6(2):115–121.
6. Murray CB, Kagan CR, Bawendi MG (2000) Synthesis and characterization of monodisperse nanocrystals and close-packed nanocrystal assemblies. *Annu Rev Mater Sci* 30:545–610.
7. Mueggenburg KE, Lin XM, Goldsmith RH, Jaeger HM (2007) Elastic membranes of close-packed nanoparticle arrays. *Nat Mater* 6(9):656–660.
8. He J, et al. (2010) Fabrication and mechanical properties of large-scale freestanding nanoparticle membranes. *Small* 6(13):1449–1456.
9. Cheng W, et al. (2009) Free-standing nanoparticle superlattice sheets controlled by DNA. *Nat Mater* 8(6):519–525.
10. Landman U, Luedtke WD (2004) Small is different: Energetic, structural, thermal, and mechanical properties of passivated nanocluster assemblies. *Faraday Discuss* 125: 1–22, discussion 99–116.
11. Salerno KM, Bolintineanu DS, Lane JMD, Grest GS (2014) High strength, molecularly thin nanoparticle membranes. *Phys Rev Lett* 113(25):258301.
12. Dreyer A, et al. (2016) Organically linked iron oxide nanoparticle supercrystals with exceptional isotropic mechanical properties. *Nat Mater* 15(5):522–528.
13. Jiang C, Markutsya S, Pikus Y, Tsukruk VV (2004) Freely suspended nanocomposite membranes as highly sensitive sensors. *Nat Mater* 3(10):721–728.
14. Kanjanaboos P, et al. (2013) Self-assembled nanoparticle drumhead resonators. *Nano Lett* 13(5):2158–2162.
15. McInnes CR (2004) *Solar Sailing: Technology, Dynamics and Mission Applications* (Springer, Berlin), pp 56–367.
16. Lin Y, et al. (2003) Ultrathin cross-linked nanoparticle membranes. *J Am Chem Soc* 125(42):12690–12691.
17. Paul DR, Robeson LM (2008) Polymer nanotechnology: Nanocomposites. *Polymer (Guildf)* 49(15):3187–3204.
18. Ye X, et al. (2015) Structural diversity in binary superlattices self-assembled from polymer-grafted nanocrystals. *Nat Commun* 6:10052.
19. Tam E, et al. (2010) Mechanical properties of face-centered cubic supercrystals of nanocrystals. *Nano Lett* 10(7):2363–2367.
20. Podsiadlo P, et al. (2010) The role of order, nanocrystal size, and capping ligands in the collective mechanical response of three-dimensional nanocrystal solids. *J Am Chem Soc* 132(26):8953–8960.
21. Lee D, et al. (2007) Viscoplastic and granular behavior in films of colloidal nanocrystals. *Phys Rev Lett* 98(2):026103.
22. Akcora P, et al. (2009) Anisotropic self-assembly of spherical polymer-grafted nanoparticles. *Nat Mater* 8(4):354–359.
23. Choi J, Dong H, Matyjaszewski K, Bockstaller MR (2010) Flexible particle array structures by controlling polymer graft architecture. *J Am Chem Soc* 132(36):12537–12539.
24. Choi J, et al. (2012) Toughening fragile matter: mechanical properties of particle solids assembled from polymer-grafted hybrid particles synthesized by ATRP. *Soft Matter* 8(15):4072–4082.
25. Schmitt M, et al. (2016) Tailoring structure formation and mechanical properties of particle brush solids via homopolymer addition. *Faraday Discuss* 186:17–30.
26. Koerner H, Drummy LF, Benicewicz B, Li Y, Vaia RA (2013) Nonisotropic self-organization of single-component hairy nanoparticle assemblies. *ACS Macro Lett* 2(8):670–676.
27. Williams GA, et al. (2015) Mechanically robust and self-healable superlattice nanocomposites by self-assembly of single-component "sticky" polymer-grafted nanoparticles. *Adv Mater* 27(26):3934–3941.
28. Milner ST (1991) Polymer brushes. *Science* 251(4996):905–914.
29. Tsujii Y, Ohno K, Yamamoto S, Goto A, Fukuda T (2006) Structure and properties of high-density polymer brushes prepared by surface-initiated living radical polymerization. *Surface-Initiated Polymerization I, Advances in Polymer Science*, ed Jordan R (Springer, Berlin), Vol 197, pp 1–45.
30. Daoud M, Cotton JP (1982) Star shaped polymers - a model for the conformation and its concentration-dependence. *J Phys* 43(3):531–538.
31. Wijmans CM, Zhulina EB (1993) Polymer brushes at curved surfaces. *Macromolecules* 26(26):7214–7224.
32. Ohno K, Morinaga T, Takeno S, Tsujii Y, Fukuda T (2007) Suspensions of silica particles grafted with concentrated polymer brush: Effects of graft chain length on brush layer thickness and colloidal crystallization. *Macromolecules* 40(25):9143–9150.
33. Dukes D, et al. (2010) Conformational transitions of spherical polymer brushes: Synthesis, characterization, and theory. *Macromolecules* 43(3):1564–1570.
34. Rubinstein M, Colby RH (2006) *Polymer Physics* (Oxford Univ Press, New York), pp 363–364.
35. Jiang Z, et al. (2015) Subnanometre ligand-shell asymmetry leads to Janus-like nanoparticle membranes. *Nat Mater* 14(9):912–917.
36. Stafford CM, et al. (2004) A buckling-based metrology for measuring the elastic moduli of polymeric thin films. *Nat Mater* 3(8):545–550.
37. Torres JM, Stafford CM, Vogt BD (2010) Impact of molecular mass on the elastic modulus of thin polystyrene films. *Polymer (Guildf)* 51(18):4211–4217.
38. Daniel IM, Ishai O (2005) *Engineering Mechanics of Composite Materials* (Oxford Univ Press, New York), 2nd Ed, pp 37–74.
39. Wang Y, et al. (2015) Strong resistance to bending observed for nanoparticle membranes. *Nano Lett* 15(10):6732–6737.
40. McFarland AW, Colton JS (2005) Role of material microstructure in plate stiffness with relevance to microcantilever sensors. *J Micromech Microeng* 15(5):1060–1067.
41. Park SK, Gao XL (2006) Bernoulli-Euler beam model based on a modified couple stress theory. *J Micromech Microeng* 16(11):2355–2359.
42. Maranganti R, Sharma P (2007) Length scales at which classical elasticity breaks down for various materials. *Phys Rev Lett* 98(19):195504.
43. Johnson WL, Samwer K (2005) A universal criterion for plastic yielding of metallic glasses with a (T/Tg) 2/3 temperature dependence. *Phys Rev Lett* 95(19):195501.
44. Ma D, et al. (2012) Elastic moduli inheritance and the weakest link in bulk metallic glasses. *Phys Rev Lett* 108(8):085501.
45. Wang WH (2012) The elastic properties, elastic models and elastic perspectives of metallic glasses. *Prog Mater Sci* 57(3):487–656.
46. Yamamoto S, Tsujii Y, Fukuda T (2002) Glass transition temperatures of high-density poly(methyl methacrylate) brushes. *Macromolecules* 35(16):6077–6079.
47. Halpin JC, Kardos JL (1976) Halpin-Tsai Equations - Review. *Polym Eng Sci* 16(5):344–352.
48. Saha R, Nix WD (2002) Effects of the substrate on the determination of thin film mechanical properties by nanoindentation. *Acta Mater* 50(1):23–38.
49. Gaulding EA, et al. (2015) Deposition of wafer-scale single-component and binary nanocrystal superlattice thin films via dip-coating. *Adv Mater* 27(18):2846–2851.